Process-dependent ferroelectric and memristive properties in polycrystalline Ca:HfO$_2$-based devices

C. Ferreyra[1], M. Badillo[2,3], M. J. Sánchez[4,5], M. Acuautla[6], B. Noheda[6,7] and D. Rubi[1]*

[1]Instituto de Nanociencia y Nanotecnología (INN), Consejo Nacional de Investigaciones Científicas y Técnicas-Comisión Nacional de Energía Atómica, nodo Constituyentes (1650), San Martín, Argentina, [2]Department of Physics, Politecnico di Milano, Milano, Italy, [3]Engineering and Technology Institute Groningen (ENTEG), University of Groningen, Groningen, Netherlands, [4]Instituto de Nanociencia y Nanotecnología (INN), CONICET-CNEA, nodo Bariloche (8400), San Carlos de Bariloche, Argentina, [5]Instituto Balseiro, UNCuyo (8400), San Carlos de Bariloche, Argentina, [6]CogniGron—Groningen Cognitive Systems and Materials Center, University of Groningen, Groningen, Netherlands, [7]Zernike Institute for Advanced Materials, University of Groningen, Groningen, Netherlands

Memristors are considered key building blocks for developing neuromorphic or in-memory computing hardware. Here, we study the ferroelectric and memristive response of Pt/Ca:HfO$_2$/Pt devices fabricated on silicon by spin-coating from chemical solution deposition followed by a pyrolysis step and a final thermal treatment for crystallization at 800°C for 90 s. For pyrolysis temperature of 300°C, the annealed samples are ferroelectric while for 400°C a dielectric behavior is observed. For each case, we found a distinct, forming-free, memristive response. Ferroelectric devices can sustain polarization switching and memristive behavior simultaneously. Aided by numerical simulations, we describe the memristive behavior of ferroelectric devices arising from oxide-metal Schottky barriers modulation by both the direction of the electrical polarization and oxygen vacancy electromigration. For non-ferroelectric samples, only the latter effect controls the memristive behavior.

KEYWORDS

ferroelectrics, memristors, oxides, oxygen vacancies, neuromorphic computation

1 Introduction

Ferroelectric materials are expected to play a key role in the development of novel nanoelectronic devices, including ferroelectric field effect transistors (FeFETs) (Park et al., 2021), ferroelectric random access memories (FeRAMs) (Scott and de Araujo, 1989), and memristive nanodevices for in-memory or neuromorphic computing (Mikolajick et al., 2023). For the latter, analog resistance changes of metal/ferroelectric/metal structures, driven by polarization switching by an external electric field, are needed to mimic the adaptive synaptic weights of biological synapses.

Ferroelectric memristive effects have been reported for perovskite materials such as BaTiO$_3$ or PZT for ultrathin oxide layers where the direction of polarization controls the tunneling currents and, therefore, the resistance of the device (the so-called Ferroelectric Tunnel Junctions, or FTJ) (Tsymbal and Kohlstedt, 2006; Garcia et al., 2009; Zhuravlev et al., 2009; Chanthbouala et al., 2012) or for thicker ferroelectric layers where the height of

the energy barrier at the interfaces with the metallic electrodes can also be tuned by the direction of polarization (Blom et al., 1994; Meyer and Waser, 2006; Pintilie et al., 2010). Electromigration of oxygen vacancies has also been shown to contribute to the memristive effect on these devices (Qian et al., 2019; Ferreyra et al., 2020a; Rengifo et al., 2022), resulting in a complex scenario with multiple entangled physical mechanisms. Reports on neuromorphic properties, such as long-term potentiation/depression and spike-timing-dependent plasticity, can already be found in the literature for these systems (Cheng et al., 2020; Kim et al., 2021; Wang et al., 2021). However, ferroelectric memristive devices based on perovskites present several drawbacks that hamper their transfer to the electronics market, such as their lack of compatibility with standard Complementary Metal Oxide Semiconductor (CMOS) processes and the presence of depolarizing effects at ultra-low thickness (Fong et al., 2004), which prevents device miniaturization down to the nanoscale.

The discovery of ferroelectric HfO_2 (hafnia)-based oxides in 2011 Böscke et al. (2011) triggered a great deal of research in the community working on oxide ferroelectrics, as this compound is CMOS compatible. Indeed, it has been used as a gate oxide in metal-oxide-semiconductor field-effect transistors (MOSFETs) since the early 2000s (Gurfinkel et al., 2006). Remarkably, it shows robust ferroelectricity for ultrathin thickness - down to 1 nm (Cheema et al., 2020)- and is also environmentally friendly. Hafnia presents a monoclinic, non-polar, lowest free energy phase; however, several metastable phases (cubic, tetragonal, orthorhombic, rhombohedral, the last two polar) can be stabilized either in nanostructured materials or in thin film form. The stabilization of polar phases depends on a complex interplay between grain size (Materlik et al., 2015; Künneth et al., 2017), the presence of cationic dopants such as Si, Al, La, Zr, Ga or Y, among others (see Ihlefeld et al., 2022 and references therein), or the presence of oxygen vacancies (Lee et al., 2008; Hoffmann et al., 2015), together with surface and strain effects (Shiraishi et al., 2016; Batra et al., 2017a). The electrodes' role in stabilizing the polar phases has been also highlighted in the literature (Böscke et al., 2011; Lin et al., 2017; Fields et al., 2020). It has been reported that the ferroelectric phase in hafnia-related polycrystalline devices is usually the orthorhombic one (Park et al., 2018), while the polar rhombohedral phase was initially shown for epitaxial $Hf_{0.5} Zr_{0.5} O_2$ films grown on $La_{2/3} Sr_{1/3} MnO_3$ buffered $SrTiO_3$ (Wei et al., 2018; Nukala et al., 2021). Most of the reported ferroelectric memristive effects in hafnia-based devices focus on the implementation of FTJ (Ambriz-Vargas et al., 2017; Wei et al., 2019; Sulzbach et al., 2020), which require stringent fabrication protocols to achieve high-quality ultrathin epitaxial oxide films with sharp, atomically controlled, interfaces with the metal electrodes.

Non-ferroelectric memristive mechanisms in hafnia-based devices point to the formation and dissolution of conducting nanofilaments of oxygen vacancies (which locally lower the material resistivity) after the application of proper electrical stimulation (Sawa, 2008; Yang et al., 2017; Sharath et al., 2017). Recently, the local core-shell structure of filaments has been disclosed by high-resolution transmission electron microscopy (Zhang et al., 2021).

Filamentary memristive effects usually require, however, an electroforming step and are characterized by steep resistance transitions (especially the one from high to low resistance, named

as SET), together with high cycle-to-cycle and device-to-device variations, arising from the stochastic nature of the filament formation process (Degraeve et al., 2015). This hinders the application of these devices in neuromorphic computing, where analog resistive changes and low cycle-to-cycle and device-to-device variations are desired for the implementation, for example, of physical neural networks based on memristor arrays organized in cross-bars (Prezioso et al., 2014). Strategies to get analog behavior with improved reliability in hafnia-based memristors, such as adding a series transistor or including in the stack an oxygen scavenging layer, have been proposed (Brivio et al., 2022; Rao et al., 2023), implying a more complex fabrication process that could impact the cost and scalability of the devices. The development of hafnia-based polycrystalline devices fabricated by scalable and low-cost procedures, displaying simultaneous ferroelectricity and forming-free memristive behavior with non-filamentary resistance modulation is therefore highly relevant for the development of new nanoelectronics.

In this paper, we study the ferroelectric and memristive response of polycrystalline Ca-doped hafnia thin films ($Ca:HfO_2$), fabricated through a scalable and green chemical method consisting on spin-coating followed by pyrolysis step and thermal treatment (Badillo et al., 2023; Badillo et al., 2024). We notice that elements of alkaline earth and lanthanides series families have been reported to be the most effective in enhancing the ferroelectric properties of doped-HfO_2 systems (Schroeder et al., 2014; Batra et al., 2017b; Schenk et al., 2019). Depending on the pyrolisis temperature, we were able to tune the ferroelectricity of the hafnia layer, which produced distinct memristive responses, easily detectable by a simple electrical characterization protocol. For pyrolisis temperature of 300°C, we obtained ferroelectric devices showing also a memristive response which, with the help of numerical simulations, we link to Schottky barrier modulation by the polarization direction coupled to oxygen vacancy dynamics. For devices pyrolized at 400°C, no ferroelectric behavior was found, together with a memristive response related solely to oxygen vacancy electromigration. In all cases, the observed scaling of the resistive states with the device area suggests area-distributed conduction paths that we locate at grain boundaries with enhanced conductivity. Our work provides valuable information about the simultaneous presence of ferroelectricity and memristive behavior in hafnia-based devices, a multifunctional behavior that could be harnessed for the development of neuromorphic or in-memory computing hardware.

2 Materials and methods

$Ca:HfO_2$ (Ca doping of 5% at.) thin films of three layers each (with a total thickness of 54 nm) were fabricated on platinized silicon substrates by spin-coating, followed by a pyrolysis step at either $T_P = 300$ or 400°C for 5 min for each layer. The films were then processed by Rapid Thermal Annealing (RTA) at 800°C for 90 s under a 0.5 atm $Ar:O_2$ atmosphere. Further information on the fabrication protocol and conditions can be found in Badillo et al. (2023) and Badillo et al. (2024). Even though our films currently require a high temperature annealing for crystallization, other approaches like fabricating doped-$HfZrO_4$ (HZO) films or using localized laser

annealing could reduce the thermal budget and/or limit the damage of underlying structures (Frank et al., 2022; Tabata et al., 2021).

Circular Pt top electrodes were fabricated by e-beam evaporation and shaped by standard UV lithography. The diameter of the top electrodes was in the range of 20–200 μm, with the most useful results recorded on devices with diameter $\leq$ 50 μm, which were less prone to electrical hard breakdown. Structural characterization was done by x-ray diffraction (XRD) in a Rigaku SmartLab XE x-ray diffractometer under in-plane incidence geometry. Electrical characterization was performed in a commercial probe station, where the bottom electrode was grounded, and electrical stimulation was applied to the top electrode. Ferroelectricity was measured at 1 kHz with an aixACCT TF 2000 Analyzer. Capacitance (C)-voltage (V) and remnant resistance (R_{REM}-V)-voltage loops were recorded in AC mode, simultaneously, with an LCR BK894 impedance analyzer, set for measuring an RC parallel circuit. This allows circumventing issues that arise from the highly insulating nature of our hafnia-based devices, which require measuring DC currents below the sensitivity of our instruments. The stimulation protocol consisted of applying alternating writing and reading DC pulses, both with a superimposed small AC signal (AC frequencies, f, ranged between 10 kHz and 1 MHz). The time-width of the writing pulses was $\tau_W \approx$ 100 ms, and their amplitudes ranged between −18 V and +18 V, with a voltage step of 300 mV. The C-V curve is constructed from the capacitance measured during the application of the writing pulses, while the remnant resistance loop is obtained from the resistances measured during the application of the reading pulses. Both the DC bias of the reading pulses and the AC amplitude were a few hundred mV.

3 Experimental results

For Ca:HfO$_2$ samples pyrolyzed at 300°C, XRD characterization -displayed in Figure 1A- shows the presence of high-symmetry fluorite phase(s) peaks (we assess that due to similar inter-planer distances, cubic, tetragonal, and polar orthorhombic polymorphs can be hardly distinguished from x-ray diffraction experiments) and negligible presence of monoclinic phase. We also observed, from specular XRD scans, that the films are preferentially oriented along the out-of-plane (001) direction, suggesting a fiber texture (Badillo et al., 2024). From atomic force microscopy (AFM) analysis (Supplementary Figure S1), root-mean-square (RMS) roughness was estimated to be 0.75 nm, with an average grain size of 79 nm. When the pyrolysis temperature of synthesis, T$_P$, is increased to 400°C, the Ca:HfO$_2$ films change their (001)-oriented fiber texture to polycrystalline, as shown by the XRD measurements displayed in Figure 1B. High-symmetry phases still make most of the Ca:HfO$_2$ film, yet evidence of monoclinic phase in small amounts is also found. A roughness of 0.52 nm and an average grain size of 102 nm were estimated for this sample (Supplementary Figure S1).

Figures 2A, B show typical current-voltage (I-V) and polarization-voltage (P-V) curves for the sample pyrolyzed at 300°C, both in their virgin state and after applying a wake-up protocol, consisting of 10^3 bipolar rectangular cycles, with an amplitude of 15 V at a frequency of 1 kHz. A dielectric behavior
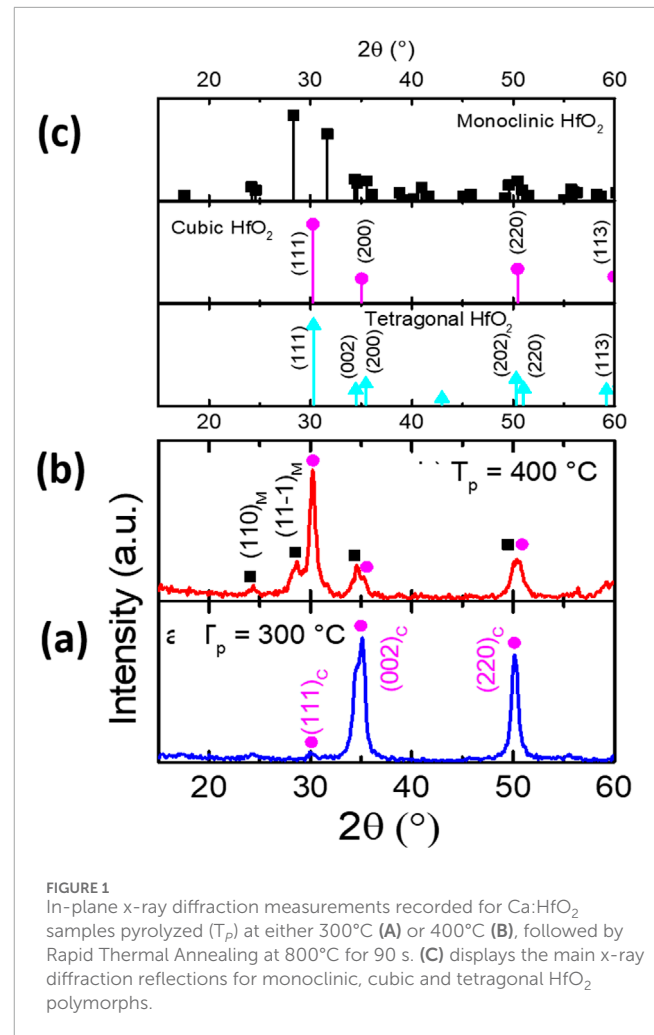
FIGURE 1
In-plane x-ray diffraction measurements recorded for Ca:HfO$_2$ samples pyrolyzed (T$_P$) at either 300°C (A) or 400°C (B), followed by Rapid Thermal Annealing at 800°C for 90 s. (C) displays the main x-ray diffraction reflections for monoclinic, cubic and tetragonal HfO$_2$ polymorphs.

is evidenced for the initial cycles, while ferroelectricity develops after the wake-up process, when a polarization of 7.2 μm/cm^2 is obtained. We notice that the wake-up process in hafnia-based systems has been associated either to oxygen vacancy redistribution between the interface(s) and the bulk oxide zone (Starschich et al., 2016) (as proved by phase contrast scanning transmission electron microscopy and energy dispersive spectroscopy experiments Chen et al., 2023) or to a phase transition between non-polar and polar polymorphs, as reported from combined in-operando Raman, photoluminescence and dark field spectroscopy (Jan et al., 2023). For the present case, we observed by transmission electron microscopy (to be reported elsewhere) that stressed devices present a hafnia layer with lower oxygen stoichiometry than the pristine film, suggesting that the ferroelectricity observed after wake-up is likely related to the growth of the polar orthorhombic phase (Badillo et al., 2023; Badillo et al., 2024) assisted by the presence of oxygen vacancies. We recall that the metastable orthorhombic phase was reported to present lower free energy in the presence of oxygen vacancies (Lee et al., 2008).

Figure 2C displays C-V and R_{REM}-V loops recorded on a similar device in its original pristine state (before any electrical stress was applied) for three consecutive full cycles. It is seen that after an erratic behavior comprising a fraction of the first cycle,
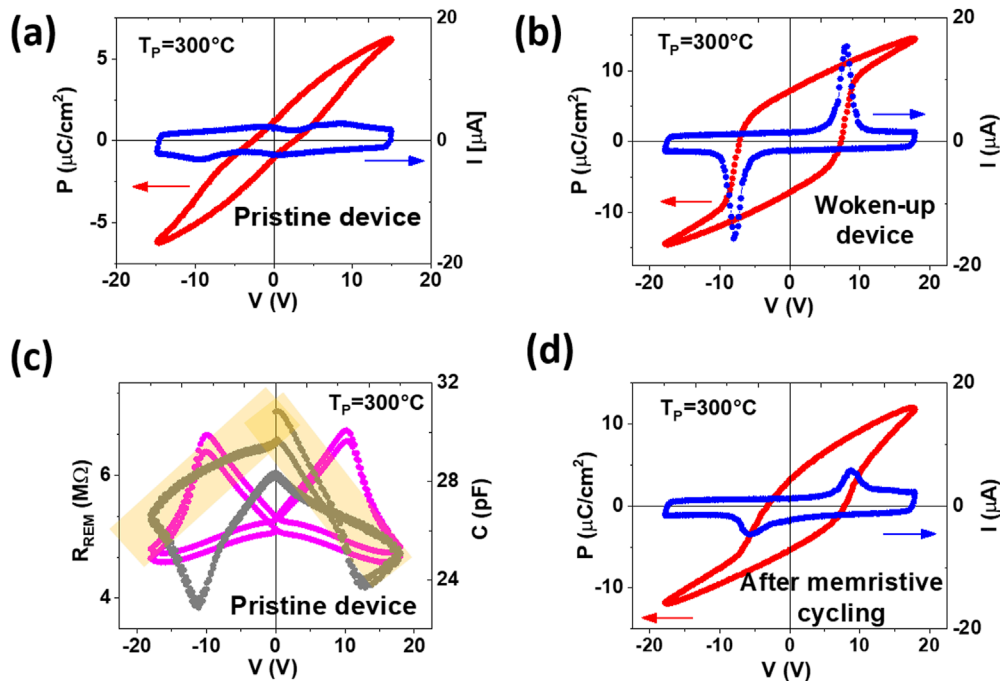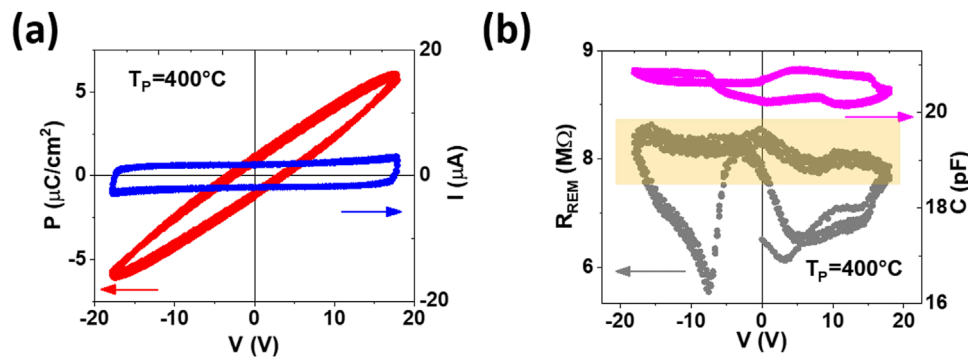
FIGURE 2
(A) Current–voltage (blue symbols) and polarization–voltage curves (red symbols) recorded on an as-prepared Pt/Ca:HfO$_2$ device (diameter 35 μm) pyrolyzed at 300°C; **(B)** Current–voltage (blue symbols) and polarization–voltage curves (red symbols) were recorded on the same device after the application of the wake-up protocol. Ferroelectricity develops after wake-up (10^3 cycles); **(C)** Capacitance–voltage (magenta symbols) and remnant resistance–voltage (gray symbols) curves recorded on an as-prepared Pt/Ca:HfO$_2$ device (with electrode diameter of 50 μm) pyrolyzed at 300°C. The AC frequency of the stimulation was 100 kHz; **(D)** Current–voltage (blue symbols) and polarization–voltage curves (red symbols) recorded on the same device, after the characterization displayed in **(C)**, where the development of ferroelectricity is also observed.

a butterfly-like C-V loop -typical response of ferroelectrics- is stabilized, indicating that a few pulses of the capacitive/memristive measurement protocol are enough to wake up the ferroelectric behavior. This is confirmed by Figure 2D, which displays I-V and P-V curves recorded afterward, showing an evident ferroelectric behavior with a polarization of 3.2 $\mu m/cm^2$, that is 45% of the polarization value obtained after waking-up, in Figure 2B. The reason why the wake-up effect is induced by a few pulses of the memristive characterization protocol relies on the longer widths of the applied pulses (100 ms per pulse) in comparison to the pulses applied during the ferroelectric wake-up (1 ms per pulse). A rough comparison between both electrical protocols (memristive and ferroelectric wake-up, respectively) shows that during one full cycle of memristive cycling, the system is stressed at an average voltage of +9 V for 12 s; on the other hand, during the ferroelectric wake-up process the system is stressed at +15 V for only 1 s, that is a time-scale one order of magnitude lower than in the previous case. This suggests that the memristive protocol is strong enough to develop ferroelectricity and likely produce some fatigue, which explains the lower polarization value observed in devices after memristive characterization vs. only woken-up devices. Also, we notice from Figure 2D the reduction of coercive voltages and the appearance of an electrical imprint in the polarization-voltage loop. The reduction of the coercive voltage upon device fatigue has also been reported for perovskite ferroelectrics and attributed to local chemical changes in the ferroelectric layer (Ievlev et al., 2019), but it can also be related

to other effects such as trapping of charges near the interfaces with the electrodes -leading to changes in the polarization screening- or structural changes involving transition between different hafnia polymorphs Jan et al. (2023). On the other hand, the development of an imprint field implies the accumulation of charges or defect dipoles during cycling that create internal bias fields that reduce the symmetry of the external coercive field (Genenko et al., 2015).

The R$_{REM}$-V loop of Figure 2C shows the presence of a pseudo-symmetric loop with a memristive butterfly that resembles an inverted C-V loop or what has also been referred to as "table-with-legs shape" (Rozenberg et al., 2010). The loop can be explained as arising from two memristive interfaces (likely the Ca:HfO$_2$/Pt ones, expected to be of Schottky-type) behaving in a complementary way (that is, when one switches from high to low resistance, the other switches inversely) (Rozenberg et al., 2010; Ferreyra et al., 2020b). We notice that the minima in the R$_{REM}$-V loop match the peaks of the C-V curve, corresponding to the coercive fields. This indicates that ferroelectric switching plays a key role in the memristive effect. We also stress that no electroforming process -usually implying a steep high-to-low resistance change- is necessary to observe this memristive effect.

Figure 3A displays I-V and P-V curves measured on a Ca:HfO$_2$ sample pyrolyzed at 400°C instead of 300°C. Noteworthily, even after the application of a wake-up process, these devices do not display ferroelectricity. Understanding the origin of the correlation between texture [(001)-oriented or polycrystalline], pyrolysis temperature,

FIGURE 3
(A) Current–voltage (blue symbols) and polarization-voltage curves (red symbols) recorded on an as-prepared Pt/Ca:HfO$_2$ device (electrode diameter 50 μm) pyrolyzed at 400°C. No changes in the dielectric response are observed after the application of the wake-up process; **(B)** Capacitance-voltage (purple symbols) and remnant resistance-voltage (gray symbols), recorded on an as-prepared Pt/Ca:HfO$_2$ device (electrode diameter 50 μm) pyrolyzed at 400°C. The AC frequency of the stimulation was 100 kHz.

and ferroelectricity is beyond the scope of the current paper and will be addressed elsewhere. The C-V and R$_{REM}$-V loops corresponding to the same device are displayed in Figure 3B. The C-V loop shows roughly constant capacitance values around 21 pF, reflecting the absence of ferroelectricity. The R$_{REM}$-V loop resembles the one obtained for the ferroelectric device but with some non-trivial differences. The main difference between the remnant loops displayed in Figures 2C, 3B relies on the top parts of the "tables," highlighted with yellow transparent bands: while the ferroelectric sample shows distinct negative (positive) slopes for positive (negative) stimulation -resembling the behavior of BaTiO$_3$ and PZT ferroelectric perovskites (Ferreyra et al., 2020a)-, the one pyrolyzed at 400°C shows reduced -closer to 0, in average-slopes. The existence of ferroelectricity gives rise to a linear voltage dependence of the resistance when the voltage is reduced from the maximum amplitude down to zero. We will discuss this in more detail later.

Further information about the memristive mechanism can be obtained from the evolution of the maximum (R$_{MAX}$) and minimum resistance (R$_{MIN}$) states, extracted from the R$_{REM}$-V loops, as a function of the device area. Figures 4A, B show these data for samples pyrolyzed at 300°C and 400°C, respectively, and for AC measuring frequencies in the range 10 kHz-1 MHz. We notice that the frequency-dependent character of R$_{REM}$ is related to the AC-mode in which we measure the resistance: R$_{REM}$ and C are measured with an LCR-meter assuming a parallel RC circuit, which is the equivalent representation of a usually more complex primary circuit linked to the different device zones (i.e., each metal/insulator interface is generally modeled by a capacitor in parallel with a resistor). In this way, the extracted R$_{REM}$ is frequency-dependent as it depends on capacitive reactances. In all cases, it is observed that R$_{MAX}$ and R$_{MIN}$ scale with the inverse of the device area, indicating that electrical transport is distributed along the entire device area. This allows discarding a memristive effect of filamentary nature, and it is consistent with the absence of a forming step, discussed above. This is surprising because filament formation is expected in materials with large bandgap, and it is, indeed, usually reported for hafnia-based devices (Yang et al., 2017; Sharath et al. 2017).

It is also seen that the R$_{MAX}$/R$_{MIN}$ ratio is consistently in the 2-3 range, which is smaller than the usually large ratios observed in filamentary-related memristive effects (Knabe et al., 2023). For completeness, Figures 4C, D display the evolution of the low voltage capacitance (extracted from the C-V curves) as a function of the device area and measuring AC frequency. For devices pyrolyzed at 300°C and 400°C, a linear scaling of the capacitance with the area is observed, in agreement with the expected behavior of a standard capacitor.

We notice that the obtained capacitance values are fully consistent with the geometrical capacitance C$_G$ of the devices given by the well-known relation

$$C_G = \epsilon_0 \epsilon_r A/d$$

where A is the device area, d the insulator layer thickness and ϵ_0 and ϵ_r are the free space permittivity and insulator dielectric constant, respectively. For instance, if we take A = 8x10^3μm^2, d = 54 nm and $\epsilon_r \approx 20$ we obtain a capacitance value C$_G \approx 26$ pF, in excellent agreement with the experimental values displayed in Figures 4A, D. As the total capacitance C of a metal/insulator/metal structure is usually given by 1/C = 1/C$_G$ + 1/C$_I$, where C$_I$ is the contribution of the insulator/metal interfaces, our observation of C $\approx$ C$_G$ implies that C$_I$ > C$_G$, setting a lower boundary for the capacitance values of the Schottky Ca:HfO$_2$/Pt interfaces present in our systems. We also stress that the capacitance values measured on our devices (in the range of pF), are lower than those found, for example, for PZT-based memristors (in the range of nF) (Ferreyra et al., 2020a). We notice that a relatively low capacitance could eventually minimize RC time constants -determining how quickly the voltage drop at the memristor rises/falls-, enabling faster switching speeds, which is essential for memory or neuromorphic computing applications.

It could be argued that the observed behavior is consistent with an interface-related memristive mechanism, where Schottky barriers present at ferroelectric/metal interfaces are modulated by both the direction of the ferroelectric polarization and oxygen vacancy electromigration (Ferreyra et al., 2020a). The highly insulating nature of hafnia (with an electronic bandgap of ≈ 6 eV)
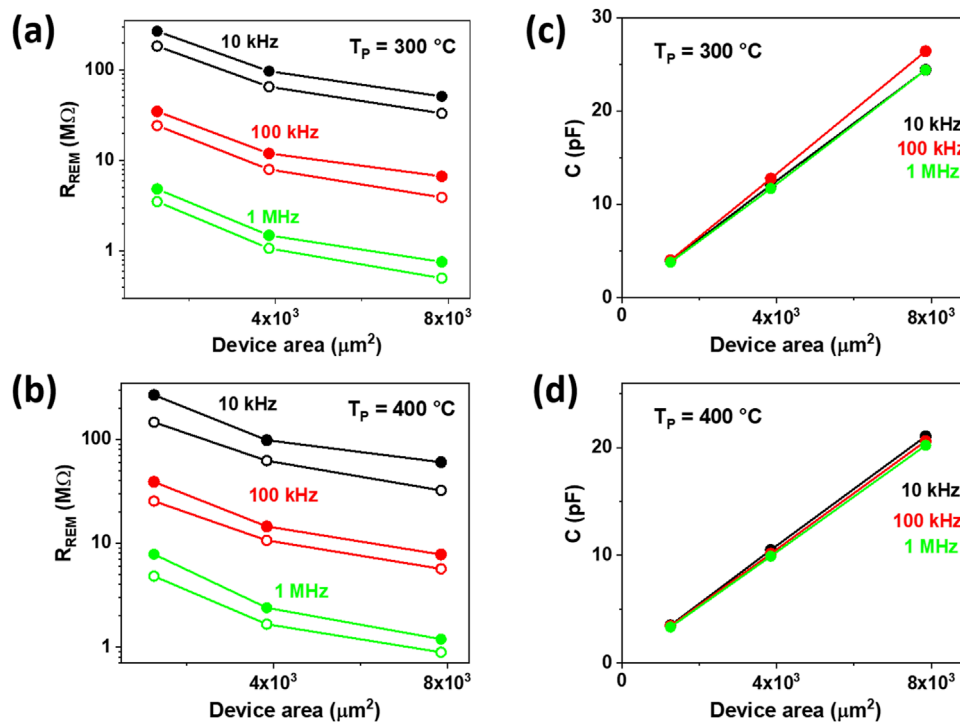
FIGURE 4
Evolution of the maximum (R_{MAX}, full circles) and minimum (R_{MAX}, open circles) remnant resistance (R_{REM}) as a function of the device area and for different AC measuring frequencies (see main text for further details about the measurement protocol), for devices pyrolyzed at **(A)** 300°C (ferroelectric devices) and **(B)** 400°C (non-ferroelectric devices). **(C, D)** display the corresponding capacitances as a function of the frequency and the device area.

suggests, however, that electronic transport might not take place homogeneously along the complete device area but that it probably occurs through grain boundaries (we recall the fiber texture and polycrystalline nature of samples pyrolyzed at 300°C and 400°C, respectively), which are usually more conducting than the bulk material (Yanev et al., 2008). In addition, it has been shown that grain boundaries behave as easy migration paths for oxygen vacancy hopping (McKenna and Shluger, 2009; Bersuker et al., 2011; Lanza et al., 2012; Xue et al., 2013). Therefore, for the case of the sample pyrolyzed at 300°C, we postulate that the observed (forming-free) memristive mechanism relies on oxygen vacancy dynamics through grain boundaries, entangled with the effect of ferroelectric polarization on the interface barrier heights. We can model this as follows.
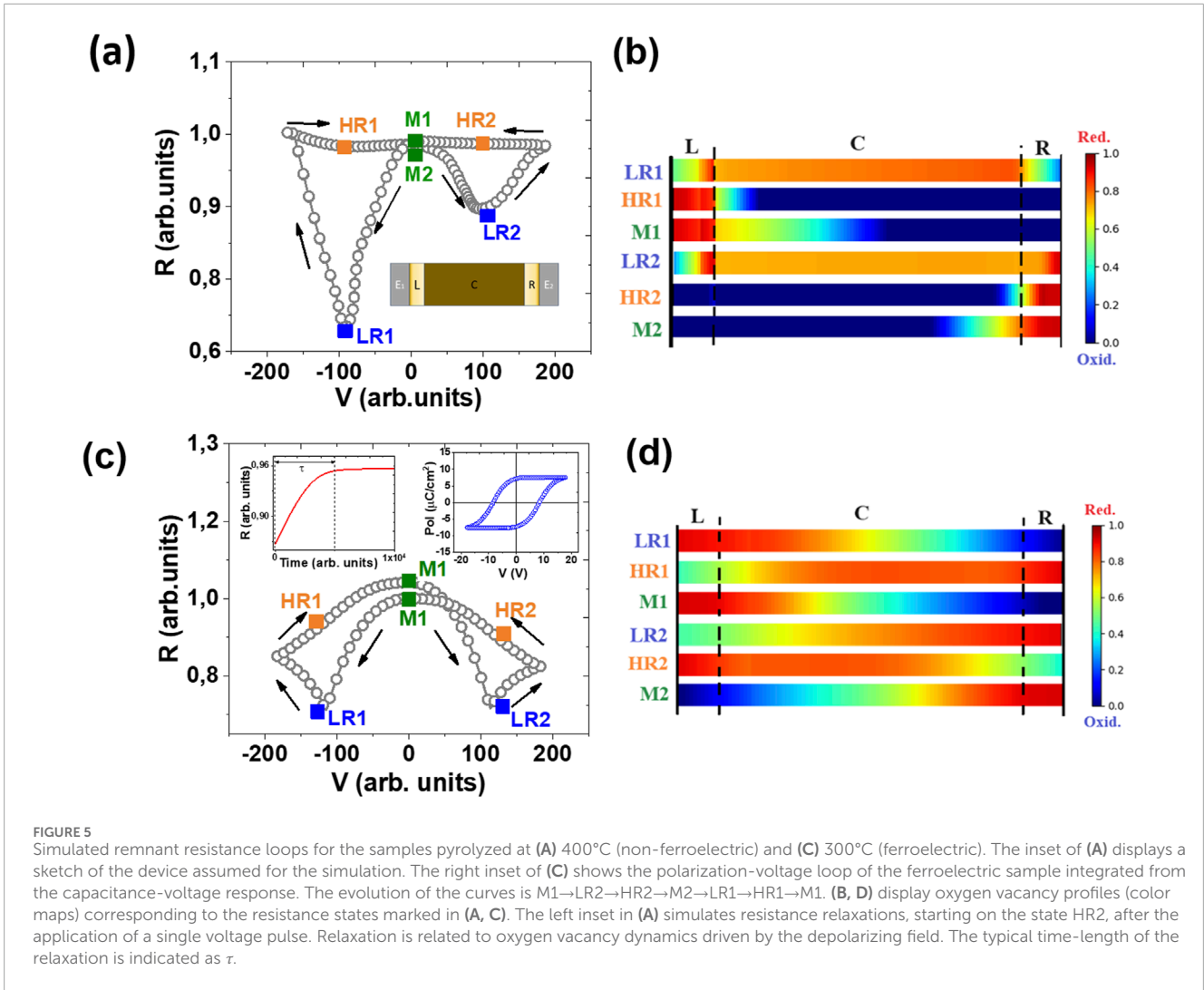
4 Memristive behavior modelling

We describe the memristive response of both samples (the ferroelectric and the non-ferroelectric one) by using the Voltage Enhanced Oxygen Drift (VEOV) (Rozenberg et al., 2010) model adapted to ferroelectric materials, developed in Ferreyra et al. (2020a) to model BaTiO$_3$ and PZT-based devices. The model assumes that the device resistance is dominated by two complementary [left (L) and right (R)] Schottky-like interfaces presenting high energy barriers. We notice that a rule of thumb is usually assumed for semiconductor/metal interfaces, which states that if the semiconductor is n-type, not diffused into the

metal, and the metal presents a high work function, then the interface is Schottky-type and the existing energy barrier should be, in any case, high. This is the case for the hafnia/Pt interface, the former being n-type and the latter presenting a high work function of around 5.6 eV. The existence of non-ohmic contacts and energy barriers at the mentioned interface has already been reported both from experiments and theoretical simulations (Kolomiiets et al., 2016; Khaldi et al., 2024).

The barrier heights are modulated both by the direction of the polarization (if it points to (from) the interface, it lowers (increases) the barrier given by the difference between the metal work function and the electron affinity of the insulating oxide) and by the local concentration of oxygen vacancies. In addition, the central zone C represents the "bulk"; of the memristive device. The inset of Figure 5A shows a sketch of the device representation used in the simulations, where L, C, and R zones are indicated.

The model assumes a 1D network of N nanodomains - formed by N$_L$ domains at the L interface, N$_R$ domains at the R interface, and N$_C$ central domains-, each one presenting a different local concentration of oxygen vacancies (δ_i) that controls the local domain resistivity (ρ_i). Vacancies can migrate to/from neighbor domains driven by the local voltage drop at the domain, which is determined by the combination of the externally applied stimulation and the depolarizing field arising from the incomplete screening of the ferroelectric bound charges (Ferreyra et al., 2020a).

FIGURE 5
Simulated remnant resistance loops for the samples pyrolyzed at **(A)** 400°C (non-ferroelectric) and **(C)** 300°C (ferroelectric). The inset of **(A)** displays a sketch of the device assumed for the simulation. The right inset of **(C)** shows the polarization-voltage loop of the ferroelectric sample integrated from the capacitance-voltage response. The evolution of the curves is M1→LR2→HR2→M2→LR1→HR1→M1. **(B, D)** display oxygen vacancy profiles (color maps) corresponding to the resistance states marked in **(A, C)**. The left inset in **(A)** simulates resistance relaxations, starting on the state HR2, after the application of a single voltage pulse. Relaxation is related to oxygen vacancy dynamics driven by the depolarizing field. The typical time-length of the relaxation is indicated as τ.

Assuming that the two-point resistance is given by Equation 1

$$R^T = R^{eff} A^{FE}(P) M^{OV}, \tag{1}$$

where R^{eff} is a scaling factor and the factor $A^{FE}(P)$ is given by Equation 2

$$A^{FE}(P) \equiv \begin{cases} \dfrac{1}{\exp(-\tilde{\gamma}_R P)} & \text{if } P \ge 0 \\[2mm] \dfrac{1}{\exp(\tilde{\gamma}_L P)} & \text{if } P < 0 \end{cases}, \tag{2}$$

Accounts for the ferroelectric modulation of oxide-metal Schottky interfaces.

In the simulations, we take P as the polarization obtained from the experimental P-V loop, being $\tilde{\gamma}_L$ and $\tilde{\gamma}_R$ parameters that account for the barrier height correction at L and R interfaces, respectively, due to the polarization (Ferreyra et al., 2020a). In addition, the prefactor M^{OV} is given by Equation 3

$$M^{OV} = N - \sum_{i=1}^{NL} A_L \delta_i - \sum_{i=NL+1}^{NL+NC} A_C \delta_i - \sum_{i=N-NR+1}^{N} A_R \delta_i, \tag{3}$$

Accounts for the oxygen vacancy dynamics, where A_i is a proportionality factor that correlates the local density of oxygen vacancies δ_i with the local resistivity ρ_i, following the relation $\rho_i \propto (1 - A_i \delta_i)$ usually considered for devices in which the local resistivity decreases with the increase in the oxygen vacancies content (and satisfying $A_i \delta_i \ll 1$ (Ghenzi et al., 2013). In the present case, we consider $A_i = A_L, A_C, A_R$, inside each region L, R and C, respectively.

Assuming an initial oxygen vacancy profile, the model allows calculating the vacancy hopping transfer rate p_{ij} between adjacent domains as shown in Equation 4

$$p_{ij} = \delta_i (1 - \delta_j) \exp(-V_0 + \Delta V_i), \tag{4}$$

with V_0 being the activation energy for vacancy hopping between neighbor domains, that we take without loss of generality as a constant along the device, and ΔV_i is the local voltage drop expressed as shown in Equation 5

$$\Delta V_i = \Delta V_i^W - \xi P, \tag{5}$$

where ΔV_i^W is due to the external write voltage (V^W), and the second term takes into account the voltage drop due to the

depolarizing field (Dawber et al., 2003) $E_{DP} = -\xi P$, with the parameter ξ tuning its strength.

After calculating the vacancy hopping rates for each simulation step, the device resistance is updated. This procedure is repeated iteratively for an external voltage ramp with symmetric voltage excursions between V_{MAX} = +1800 arb. units and V_{MIN} = −1800 arb. units (20 arb. units correspond to ≈ 1 V), respectively, until a full R-V^W loop is obtained. The time-width of the write pulses was set in 10 arb. units, which corresponds to ≈ 100 ms. We refer to Ferreyra et al. (2020a) for further details on the model and its implementation.

Figure 5A shows the simulated remnant resistance loop corresponding to the device pyrolyzed at 400°C (non-ferroelectric). For this sample, A^{FE} = 1 was assumed. The numerical values given to the model parameters are shown in the Supplementary Table S1. The simulated remnant resistance loop displays a "table-with-legs" shape that comprises the main features observed experimentally (see Figure 3B); in particular, the top part of the "table" is flat, reflecting the time stability of the high resistance state. The asymmetry between positive and negative stimulation resembles the experimental loop (recall Figure 3B). It is related to the fact that, despite the nominal symmetry of both ferroelectric/metal interfaces, they present different thermal histories -the bottom interface (R in the sketch of Figure 5A) was annealed at high temperature while the top one (L in the sketch), fabricated *ex-situ*, was not-. The asymmetry between both interfaces is taken into account by our model by giving slightly different values to the A_L and A_R parameters (see Supplementary Table S1). We also notice that $A_L, A_R > A_C$, which is necessary to warrant a higher resistivity in the zones close to the interfaces (L and R) compared to the central (C) zone, consistently with their Schottky nature.

Figure 5B shows oxygen vacancy density heat maps corresponding to the resistance states indicated in Figure 5A. We stress that, in this case, the memristive behavior is solely related to the internal vacancy electromigration between L and R interfaces, as it was shown in standard memristive systems such as manganites (Rozenberg et al., 2010) or TiO_x and TaO_x-based (Ghenzi et al., 2014; Ferreyra et al., 2020a) devices.

Figure 5C displays the simulated remnant resistance loop corresponding to the ferroelectric device. In this case, the A^{FE} factor was considered as in Equation 2. The P-V loop, used as an input for the calculation of A^{FE}, is displayed as an inset and was obtained after time integration of the experimental C-V response. The simulated remnant resistance loop presents the following features, in line with the experimental loop displayed in Figure 2C: i) the "legs" of the "table" match the coercive fields, reflecting that polarization reversal plays a fundamental role in the memristive effect; ii) the top part of the "table" displays non-zero slopes, which are an indication of resistance relaxations (volatile effect) in the absence of external stimulation. This is further addressed below.

The numerical values used in modeling the remnant resistance loop of Figure 5C are listed in Supplementary Table S1. Figure 5D displays oxygen vacancy density heat maps corresponding to the resistance states indicated in the remnant resistance loop of Figure 5C. The comparison with the non-ferroelectric device (Figure 5B) suggests softer oxygen vacancy profiles for the ferroelectric case (milder color gradients). This can be explained in terms of the competing effects on oxygen

vacancy dynamics due to both the external electric field and E_{DP}. For instance, a positive external voltage applied to the electrode next to the L interface intends to move (positively charged) vacancies towards the R interface; however, as the sample is polarized pointing to the R interface, the E_{DP} points to the opposite direction and, therefore, tries to pump vacancies towards the L interface, competing with the effect of the external stimulation.

The left inset of Figure 5C simulates the evolution of the resistance under zero external voltage for a ferroelectric device initially set in the HR2 state of Figure 5C. It confirms the presence of resistance relaxations under zero external bias, with a progressive resistance increase with a characteristic time $\tau \approx 5x10^3$ arb. units, which corresponds to ≈ 50 s. The relaxation is similar to what was experimentally found in PZT-based devices (Ferreyra et al., 2020a), and it is related to oxygen vacancy dynamics driven by the depolarizing field E_{DP} (recall Equation 5).

We notice that the existence of a robust E_{DP} in hafnia-related oxides remains controversial. It can be argued that the relatively high polarization found in ultra-thin hafnia films might originate from a low E_{DP}, possibly screened by point defects such as oxygen vacancies. However, other reports suggest the existence of a strong E_{DP} in hafnia-based devices (Kim et al., 2023). Our results are more aligned with the latter scenario, as it assumes the presence of a E_{DP} strong enough to participate in oxygen vacancy dynamics but lower than the coercive field, avoiding in this way depolarization effects.

In the Supplementary Material we include additional simulations showing how the resistance time relaxations can be exploited for the implementation of a neuromorphic algorithm for time-series classification.

5 Conclusion

In summary, we have fabricated and electrically characterized Ca-doped hafnia-based devices, synthesized by a simple chemical solution method consisting in spin-coating, pyrolysis and rapid thermal annealing. Both the ferroelectric and memristive properties can be tailored by subtly modifying fabrication parameters such as the pyrolysis temperature. For pyrolisis temperature of 300°C we obtain ferroelectric devices with a distinct memristive response related to Schottky barrier modulation by both the direction of the ferroelectric polarization and oxygen vacancy dynamics. For samples pyrolyzed at 400°C, no ferroelectric behavior was observed and the memristive behavior was solely related to electromigration of oxygen vacancies. Unlike other reports on hafnia-based memristors, our devices are forming-free and show area-dependent memristive behavior, which is inconsistent with filament formation. The devices display simultaneously ferroelectricity and memristive behavior, unlike previous reports on epitaxial samples, which showed that the two effects occur independently (Knabe et al., 2023). In the absence of external stimulation, resistance relaxations occur, an effect that could be exploited for the development of neuromorphic hardware.

Data availability statement

The raw data supporting the conclusions of this article will be made available by the authors, without undue reservation.

Author contributions

CF: Investigation, Data Curation, Writing–review and editing. MB: Investigation, Writing–review and editing. MS: Writing–review and editing. MA: Writing–review and editing. BN: Writing–review and editing, Funding adquisition. DR: Writing–original draft, Funding adquisition.

Funding

Conflict of interest

The authors declare that the research was conducted in the absence of any commercial or financial relationships that could be construed as a potential conflict of interest.

Publisher's note

All claims expressed in this article are solely those of the authors and do not necessarily represent those of their affiliated organizations, or those of the publisher, the editors and the reviewers. Any product that may be evaluated in this article, or claim that may be made by its manufacturer, is not guaranteed or endorsed by the publisher.

Supplementary material

The Supplementary Material for this article can be found online at: https://www.frontiersin.org/articles/10.3389/fmats.2024.1501000/full#supplementary-material

References

Ambriz-Vargas, F., Kolhatkar, G., Broyer, M., Hadj-Youssef, A., Nouar, R., Sarkissian, A., et al. (2017). A complementary metal oxide semiconductor process-compatible ferroelectric tunnel junction. *ACS Appl. Mater. Interfaces* 9, 13262–13268. doi:10.1021/acsami.6b16173

Badillo, M., Taleb, S., Carreno Jimenez, B., Mokabber, T., Castanedo Pérez, R., Torres-Delgado, G., et al. (2024). (001)-oriented sr:hfo2 ferroelectric films deposited by a flexible chemical solution method. *ACS Appl. Electron. Mater.* 6, 1809–1820. doi:10.1021/acsaelm.3c01725

Badillo, M., Taleb, S., Mokabber, T., Rieck, J., Castanedo, R., Torres, G., et al. (2023). Low-toxicity chemical solution deposition of ferroelectric ca:hfo2. *J. Mater. Chem. C* 11, 1119–1133. doi:10.1039/D2TC04182K

Batra, R., Huan, T. D., Jones, J. L., Rossetti, G., and Ramprasad, R. (2017a). Factors favoring ferroelectricity in hafnia: a first-principles computational study. *J. Phys. Chem. C* 121, 4139–4145. doi:10.1021/acs.jpcc.6b11972

Batra, R., Huan, T. D., Rossetti, G. A. J., and Ramprasad, R. (2017b). Dopants promoting ferroelectricity in hafnia: insights from a comprehensive chemical space exploration. *Chem. Mater.* 29, 9102–9109. doi:10.1021/acs.chemmater.7b02835

Bersuker, G., Yum, J., Vandelli, L., Padovani, A., Larcher, L., Iglesias, V., et al. (2011). Grain boundary-driven leakage path formation in hfo2 dielectrics. *Solid-State Electron.* 65-66, 146–150. doi:10.1016/j.sse.2011.06.031

Blom, P. W. M., Wolf, R. M., Cillessen, J. F. M., and Krijn, M. P. C. M. (1994). Ferroelectric Schottky diode. *Phys. Rev. Lett.* 73, 2107–2110. doi:10.1103/physrevlett.73.2107

Böscke, T. S., Müller, J., Bräuhaus, D., Schröder, U., and Böttger, U. (2011). Ferroelectricity in hafnium oxide thin films. *Appl. Phys. Lett.* 99, 102903. doi:10.1063/1.3634052

Brivio, S., Spiga, S., and Ielmini, D. (2022). Hfo2-based resistive switching memory devices for neuromorphic computing. *Neuromorphic Comput. Eng.* 2, 042001. doi:10.1088/2634-4386/ac9012

Chanthbouala, A., Garcia, V., Cherifi, R. O., Bouzehouane, K., Fusil, S., Moya, X., et al. (2012). A ferroelectric memristor. *Nat. Mater* 11, 860–864. doi:10.1038/nmat3415

Cheema, S. S., Kwon, D., Shanker, N., dos Reis, R., Hsu, S.-L., Xiao, J., et al. (2020). Enhanced ferroelectricity in ultrathin films grown directly on silicon. *Nature* 580, 478–482. doi:10.1038/s41586-020-2208-x

Chen, L., Liang, Z., Shao, S., Huang, Q., Tang, K., and Huang, R. (2023). First direct observation of the built-in electric field and oxygen vacancy migration in ferroelectric hf0.5zr0.5o2 film during electrical cycling. *Nanoscale* 15, 7014–7022. doi:10.1039/d2nr06582g

Cheng, S., Fan, Z., Rao, J., Hong, L., Huang, Q., Tao, R., et al. (2020). Highly controllable and silicon-compatible ferroelectric photovoltaic synapses for neuromorphic computing. *iScience* 23, 101874. doi:10.1016/j.isci.2020.101874

Dawber, M., Chandra, P., Litlewwod, P. B., and Scott, J. (2003). Depolarization corrections to the coercive field in thin-film ferroelectrics. *J. Phys. Condens. Matter* 15, L393. doi:10.1088/0953-8984/15/24/106

Degraeve, R., Fantini, A., Raghavan, N., Goux, L., Clima, S., Govoreanu, B., et al. (2015). Causes and consequences of the stochastic aspect of filamentary rram. *Microelectron. Eng.* 147, 171–175. Insulating Films on Semiconductors 2015. doi:10.1016/j.mee.2015.04.025

Ferreyra, C., Rengifo, M., Sánchez, M., Everhardt, A., Noheda, B., and Rubi, D. (2020a). Key role of oxygen-vacancy electromigration in the memristive response of ferroelectric devices. *Phys. Rev. Appl.* 14, 044045. doi:10.1103/physrevapplied.14.044045

Ferreyra, C., Sánchez, M., Aguirre, M., Acha, C., Bengió, S., Lecourt, J., et al. (2020b). Selective activation of memristive interfaces in TaO$_x$-based devices by controlling oxygen vacancies dynamics at the nanoscale. *Nanotechnology* 31, 155204. doi:10.1088/1361-6528/ab6476

Fields, S. S., Smith, S. W., Ryan, P. J., Jaszewski, S. T., Brummel, I. A., Salanova, A., et al. (2020). Phase-exchange-driven wake-up and fatigue in ferroelectric hafnium zirconium oxide films. *ACS Appl. Mater. Interfaces* 12, 26577–26585. doi:10.1021/acsami.0c03570

Fong, D. D., Stephenson, G. B., Streiffer, S. K., Eastman, J. A., Auciello, O., Fuoss, P. H., et al. (2004). Ferroelectricity in ultrathin perovskite films. *Science* 304, 1650–1653. doi:10.1126/science.1098252

Frank, M. M., Cartier, E. A., Lavoie, C., Carr, A., Jordan-Sweet, J. L., Jamison, P. C., et al. (2022). "Crystallization of hafnium-oxide-based ferroelectrics for beol integration," in *2022 6th IEEE electron devices Technology manufacturing conference (EDTM)*, 316–318.

Garcia, V., Fusil, S., Bouzehouane, K., Enouz-Vedrenne, S., Mathur, N. D., Barthelemy, A., et al. (2009). Giant tunnel electroresistance for non-destructive readout of ferroelectric states. *Nature* 460, 81–84. doi:10.1038/nature08128

Genenko, Y. A., Glaum, J., Hoffmann, M. J., and Albe, K. (2015). Mechanisms of aging and fatigue in ferroelectrics. *Mater. Sci. Eng. B* 192, 52–82. doi:10.1016/j.mseb.2014.10.003

Ghenzi, N., Sánchez, M. J., and Levy, P. (2013). A compact model for binary oxides-based memristive interfaces. *J. Phys. D. Appl. Phys.* 46, 415101. doi:10.1088/0022-3727/46/41/415101

Ghenzi, N., Sánchez, M. J., Rubi, D., Rozenberg, M. J., Urdaniz, C., Weissman, M., et al. (2014). Tailoring conductive filaments by electroforming polarity in memristive based TiO2 junctions. *Appl. Phys. Lett.* 104, 183505. doi:10.1063/1.4875559

Gurfinkel, M., Suehle, J., Bernstein, J., and Shapira, Y. (2006). "Enhanced gate induced drain leakage current in hfo2 mosfets due to remote interface trap-assisted tunneling," in *2006 international electron devices meeting*, 1–4. doi:10.1109/IEDM.2006.346896

Hoffmann, M., Schroeder, U., Schenk, T., Shimizu, T., Funakubo, H., Sakata, O., et al. (2015). Stabilizing the ferroelectric phase in doped hafnium oxide. *J. Appl. Phys.* 118, 072006. doi:10.1063/1.4927805

Ievlev, A. V., Kc, S., Vasudevan, R. K., Kim, Y., Lu, X., Alexe, M., et al. (2019). Non-conventional mechanism of ferroelectric fatigue via cation migration. *Nat. Commun.* 10, 3064. doi:10.1038/s41467-019-11089-w

Ihlefeld, J. F., Jaszewski, S. T., and Fields, S. S. (2022). A Perspective on ferroelectricity in hafnium oxide: mechanisms and considerations regarding its stability and performance. *Appl. Phys. Lett.* 121, 240502. doi:10.1063/5.0129546

Jan, A., Rembert, T., Taper, S., Symonowicz, J., Strkalj, N., Moon, T., et al. (2023). In operando optical tracking of oxygen vacancy migration and phase change in few nanometers ferroelectric hzo memories. *Adv. Funct. Mater.* 33, 2214970. doi:10.1002/adfm.202214970

Khaldi, O., Zemzemi, M., Ferhi, H., and Jomni, F. (2024). Relationship between electrode material, valence band offset, and nonlinearity in the resistive switching behavior of au/hfo2/m (m=tin, w, pt, or alcu) metal–insulator–metal devices: Correlation between experimental and dft calculations. *J. Electr. Mater.* 53, 4357–4369. doi:10.1007/s11664-024-11206-6

Kim, D., Heo, S. J., Pyo, G., Choi, H. S., Kwon, H.-J., and Jang, J. E. (2021). Pzt ferroelectric synapse tft with multi-level of conductance state for neuromorphic applications. *IEEE Access* 9, 140975–140982. doi:10.1109/ACCESS.2021.3119607

Kim, D., Kim, J., Yun, S., Lee, J., Seo, E., and Kim, S. (2023). Ferroelectric synaptic devices based on CMOS-compatible HfAlO$_x$for neuromorphic and reservoir computing applications. *Nanoscale* 15, 8366–8376. doi:10.1039/d3nr01294h

Knabe, J., Berg, F., Thorben Go, K., Boettger, U., and Dittmann, R. (2023). Dual-mode operation of epitaxial hf0.5zr0.5o2: ferroelectric and filamentary-type resistive switching. *Phys. status solidi (a)* 221, 2300409. doi:10.1002/pssa.202300409

Kolomiiets, N. M., Afanas'ev, V. V., Opsomer, K., Houssa, M., and Stesmans, A. (2016). Hydrogen induced dipole at the pt/oxide interface in mos devices. *Phys. status solidi (a)* 213, 260–264. doi:10.1002/pssa.201532413

Künneth, C., Materlik, R., and Kersch, A. (2017). Modeling ferroelectric film properties and size effects from tetragonal interlayer in Hf1−xZrxO2 grains. *J. Appl. Phys.* 121, 205304. doi:10.1063/1.4983811

Lanza, M., Zhang, K., Porti, M., Nafría, M., Shen, Z. Y., Liu, L. F., et al. (2012). Grain boundaries as preferential sites for resistive switching in the HfO2 resistive random access memory structures. *Appl. Phys. Lett.* 100, 123508. doi:10.1063/1.3697648

Lee, C.-K., Cho, E., Lee, H.-S., Hwang, C. S., and Han, S. (2008). First-principles study on doping and phase stability of hfo2. *Phys. Rev. B* 78, 012102. doi:10.1103/PhysRevB.78.012102

Lin, Y.-C., McGuire, F., and Franklin, A. D. (2017). Realizing ferroelectric Hf0.5Zr0.5O2 with elemental capping layers. *J. Vac. Sci. Technol. B* 36, 011204. doi:10.1116/1.5002558

Materlik, R., Künneth, C., and Kersch, A. (2015). The origin of ferroelectricity in Hf1xZrxO2: a computational investigation and a surface energy model. *J. Appl. Phys.* 117, 134109. doi:10.1063/1.4916707

McKenna, K., and Shluger, A. (2009). The interaction of oxygen vacancies with grain boundaries in monoclinic HfO2. *Appl. Phys. Lett.* 95, 222111. doi:10.1063/1.3271184

Meyer, R., and Waser, R. (2006). Hysteretic resistance concepts in ferroelectric thin films. *J. Appl. Phys.* 100, 051611. doi:10.1063/1.2337078

Mikolajick, T., Park, M. H., Begon-Lours, L., and Slesazeck, S. (2023). From ferroelectric material optimization to neuromorphic devices. *Adv. Mater.* 35, 2206042. doi:10.1002/adma.202206042

Nukala, P., Ahmadi, M., Wei, Y., de Graaf, S., Stylianidis, E., Chakrabortty, T., et al. (2021). Reversible oxygen migration and phase transitions in hafnia-based ferroelectric devices. *Science* 372, 630–635. doi:10.1126/science.abf3789

Park, H. W., Lee, J.-G., and Hwang, C. S. (2021). Review of ferroelectric field-effect transistors for three-dimensional storage applications. *Nano Sel.* 2, 1187–1207. doi:10.1002/nano.202000281

Park, M. H., Lee, Y. H., Mikolajick, T., Schroeder, U., and Hwang, C. S. (2018). Review and perspective on ferroelectric hfo2-based thin films for memory applications. *MRS Commun.* 8, 795–808. doi:10.1557/mrc.2018.175

Pintilie, L., Stancu, V., Trupina, L., and Pintilie, I. (2010). Ferroelectric Schottky diode behavior from a SrRuO3-Pb(Zr0.2Ti0.8)O3-Ta structure. *Phys. Rev. B* 82, 085319. doi:10.1103/physrevb.82.085319

Prezioso, M., Merrikh-Bayat, F., Hoskins, B., Adam, G., Likharev, K., and Strukov, D. (2014). Training and operation of an integrated neuromorphic network based on metal-oxide memristors. *Nature* 521, 61–64. doi:10.1038/nature14441

Qian, M., Fina, I., Sulzbach, M. C., Sánchez, F., and Fontcuberta, J. (2019). Synergetic electronic and ionic contributions to electroresistance in ferroelectric capacitors. *Adv. Electr. Mater.* 5, 1800646. doi:10.1002/aelm.201800646

Rao, M., Tang, H., Wu, J., Song, W., Zhang, M., Yin, W., et al. (2023). Thousands of conductance levels in memristors integrated on CMOS. *Nature* 615, 823–829. doi:10.1038/s41586-023-05759-5

Rengifo, M., Aguirre, M. H., Sirena, M., Lüders, U., and Rubi, D. (2022). Epitaxial ferroelectric memristors integrated with silicon. *Front. Nanotechnol.* 4. doi:10.3389/fnano.2022.1092177

Rozenberg, M. J., Sánchez, M. J., Weht, R., Acha, C., Gomez-Marlasca, F., and Levy, P. (2010). Mechanism for bipolar resistive switching in transition-metal oxides. *Phys. Rev. B* 81, 115101. doi:10.1103/physrevb.81.115101

Sawa, A. (2008). Resistive switching in transition metal oxides. *Mater. Today* 11, 28–36. doi:10.1016/s1369-7021(08)70119-6

Schenk, T., Fancher, C. M., Park, M. H., Richter, C., Künneth, C., Kersch, A., et al. (2019). On the origin of the large remanent polarization in la:hfo2. *Adv. Electron. Mater.* 5, 1900303. doi:10.1002/aelm.201900303

Schroeder, U., Yurchuk, E., Müller, J., Martin, D., Schenk, T., Polakowski, P., et al. (2014). Impact of different dopants on the switching properties of ferroelectric hafniumoxide. *Jpn. J. Appl. Phys.* 53, 08LE02. doi:10.7567/jjap.53.08le02

Scott, J. F., and de Araujo, C. A. P. (1989). Ferroelectric memories. *Science* 246, 1400–1405. doi:10.1126/science.246.4936.1400

Sharath, S. U., Vogel, S., Molina-Luna, L., Hildebrandt, E., Wenger, C., Kurian, J., et al. (2017). Control of switching modes and conductance quantization in oxygen engineered HfO$_x$ based memristive devices. *Adv. Funct. Mater.* 27, 1700432. doi:10.1002/adfm.201700432

Shiraishi, T., Katayama, K., Yokouchi, T., Shimizu, T., Oikawa, T., Sakata, O., et al. (2016). Impact of mechanical stress on ferroelectricity in (Hf0.5Zr0.5)O2 thin films. *Appl. Phys. Lett.* 108, 262904. doi:10.1063/1.4954942

Starschich, S., Menzel, S., and Böttger, U. (2016). Evidence for oxygen vacancies movement during wake-up in ferroelectric hafnium oxide. *Appl. Phys. Lett.* 108, 032903. doi:10.1063/1.4940370

Sulzbach, M. C., Estandía, S., Long, X., Lyu, J., Dix, N., Gàzquez, J., et al. (2020). Unraveling ferroelectric polarization and ionic contributions to electroresistance in epitaxial hf0.5zr0.5o2 tunnel junctions. *Adv. Electron. Mater.* 6, 1900852. doi:10.1002/aelm.201900852

Tabata, T., Halty, S., Rozé, F., Huet, K., and Mazzamuto, F. (2021). Non-doped hfo2 crystallization controlled by dwell time in laser annealing. *Appl. Phys. Express* 14, 115503. doi:10.35848/1882-0786/ac2c18

Tsymbal, E. Y., and Kohlstedt, H. (2006). Tunneling across a ferroelectric. *Science* 313, 181–183. doi:10.1126/science.1126230

Wang, C., Agrawal, A., Yu, E., and Roy, K. (2021). Multi-level neuromorphic devices built on emerging ferroic materials: a review. *Front. Neurosci.* 15, 661667. doi:10.3389/fnins.2021.661667

Wei, Y., Matzen, S., Quinteros, C. P., Maroutian, T., Agnus, G., Lecoeur, P., et al. (2019). Magneto-ionic control of spin polarization in multiferroic tunnel junctions. *npj Quantum Mater* 4, 62. doi:10.1038/s41535-019-0201-0

Wei, Y., Nukala, P., Salverda, M., Matzen, S., Zhao, H. J., Momand, J., et al. (2018). A rhombohedral ferroelectric phase in epitaxially strained Hf0.5Zr0.5O2 thin films. *Nat. Mater* 17, 1095–1100. doi:10.1038/s41563-018-0196-0

Xue, K.-H., Blaise, P., Fonseca, L. R. C., Molas, G., Vianello, E., Traoré, B., et al. (2013). Grain boundary composition and conduction in HfO2: an *ab initio* study. *Appl. Phys. Lett.* 102, 201908. doi:10.1063/1.4807666

Yanev, V., Rommel, M., Lemberger, M., Petersen, S., Amon, B., Erlbacher, T., et al. (2008). Tunneling atomic-force microscopy as a highly sensitive mapping tool for the characterization of film morphology in thin high-k dielectrics. *Appl. Phys. Lett.* 92, 252910. doi:10.1063/1.2953068

Yang, Y., Zhang, X., Qin, L., Zeng, Q., Qiu, X., and Huang, R. (2017). Probing nanoscale oxygen ion motion in memristive systems. *Nat. Commun.* 8, 15173. doi:10.1038/ncomms15173

Zhang, Y., Mao, G.-Q., Zhao, X., Li, Y., Zhang, M., Wu, Z., et al. (2021). Evolution of the conductive filament system in hfo2-based memristors observed by direct atomic-scale imaging. *Nat. Commun.* 12, 7232. doi:10.1038/s41467-021-27575-z

Zhuravlev, M. Y., Wang, Y., Maekawa, S., and Tsymbal, E. Y. (2009). Tunneling electroresistance in ferroelectric tunnel junctions with a composite barrier. *Appl. Phys. Lett.* 95, 052902. doi:10.1063/1.3195075